Materials and Structures (2024) 57:91
https://doi.org/10.1617/s11527-024-02374-2

ORIGINAL ARTICLE

Predicting the impact of water transport on carbonation-induced corrosion in variably saturated reinforced concrete

Evžen Korec · Lorenzo Mingazzi · Francesco Freddi · Emilio Martínez-Pañeda

Received: 21 November 2023 / Accepted: 21 April 2024

Abstract A modelling framework for predicting carbonation-induced corrosion in reinforced concrete is presented. The framework constituents include a new model for water transport in cracked concrete, a link between corrosion current density and water saturation, and a theory for characterising concrete carbonation. The theoretical framework is numerically implemented using the finite element method and model predictions are extensively benchmarked against experimental data. The results show that the model is capable of accurately predicting carbonation progress, as well as wetting and drying of cracked and uncracked concrete, revealing a very good agreement with independent experiments from a set of consistent parameters. In addition, insight is gained into the evolution of carbonation penetration and corrosion current density under periodic wetting and drying conditions. Among others, we find that cyclic wetting periods significantly speed up the carbonation progress and that the induced corrosion current density is very sensitive to concrete saturation.

Keywords Concrete · Carbonation · Modeling · Finite element analysis · Degradation · Permeability

1 Introduction

This study presents a new model for predicting carbonation corrosion in reinforced concrete subjected to variable moisture saturation. Carbonation results from the penetration of atmospheric carbon dioxide (CO_2) into concrete, leading to a series of chemical reactions involving the transformation of calcium hydroxide into calcium carbonate, which causes acidification of the basic concrete pore solution [1–3]. This pH drop is known to destabilise the protective passive layer on the surface of steel rebars, triggering rebar corrosion [1]. Corrosion of steel rebars is the main deterioration mechanism of concrete structures, being responsible for the premature degradation of 70–90% of them [4, 5]. Also, carbonation can negatively affect the freeze-thaw resistance and can lead to the shrinkage of concrete [6]. On the other hand, it can also have some positive effects such as the enhancement of mechanical properties of concrete made from Portland cement, crack self-healing [7], increased resistance to low-temperature sulfate attack[8] or the removal of carbon dioxide from the atmosphere [6].

E. Korec · E. Martínez-Pañeda
Department of Civil and Environmental Engineering, Imperial College London, SW7 2AZ, London, UK

L. Mingazzi · F. Freddi
Department of Engineering and Architecture, Universitá degli Studi di Parma, Parco Area delle Scienze 181/A, Parma 43124, Italy

E. Martínez-Pañeda (✉)
Department of Engineering Science, University of Oxford, OX1 3PJ, Oxford, UK
e-mail: emilio.martinez-paneda@eng.ox.ac.uk

Published online: 04 May 2024

Concrete carbonation has been one of the major concerns for researchers aiming at reducing carbon emissions by developing new low-carbon binders, where a significant portion of clinker (ordinary Portland cement) is replaced with supplementary cementitious materials such as fly-ash, limestone, and geopolymers. Although the resulting material has a lower environmental footprint, lower calcium hydroxide content leads to a reduced concrete pH buffer capacity and a higher susceptibility to carbonation [6, 9–11].

Concrete water saturation and microstructure play a dominant role in the carbonation process [1, 6, 12]. Low levels of water saturation facilitate the penetration of atmospheric carbon dioxide into concrete but the reaction proceeds in pore solution and thus its rate increases with concrete water saturation [1]. Also, carbonation affects the concrete microstructure and consequently the water permeability of concrete in a complex, and so far not entirely understood, way. In Portland cement, carbonation-induced pore clogging was found to prevail over micro-cracking, reducing permeability, while for concretes made from blended cements the opposite was observed [13].

For these reasons, the interaction of carbonation and water transport has been intensively studied and a number of models have been proposed. Although some early models initially did not explicitly consider water transport [14], many coupled models have been introduced since [15–21]. Seigneur et al. [22, 23] conducted detailed reactive transport modelling of carbonation considering the role of various mineral phases of cement paste. Bretti et al. [24] numerically investigated the interplay between carbonation in Portland cement and pore water content, as well as the porosity variation resulting from the carbonation process. Nguyen et al. [25] formulated a coupled model that explicitly resolved the mesoscale nature of concrete. Although diffusion is typically the dominant transport mechanism of carbon dioxide in concrete [26], advection under high hydrostatic pressure could also play a role, for example in the case of radioactive waste disposal underground concrete structures, as studied by [27]. Kari et al. [28] used a coupled model to show that extrapolation based on a linear diffusion equation was too simplistic to describe the kinetics involved in long-term carbonation. The combined effect of carbonation and chloride attack was investigated by [29–32] and [33]. Recently, Freddi and Mingazzi [34] coupled carbonation and fracture by means of a phase field model, allowing for the investigation of the interaction between carbonation and the corrosion-induced cracking process that is triggered by carbonation, but without incorporating the role of moisture. Developing models capable of resolving the interplay between cracks, carbonation, water content and corrosion is critical to deliver service life predictions; yet this is an area that remains to be explored. In particular, there is a need for models capable of capturing the role that cracks play in accelerating water transport, as this is arguably a dominant contribution [35].

In this work, we present a new theoretical and computational framework that accounts for: (i) the transport of water through bulk and cracked concrete, (ii) the interplay between water saturation and corrosion current density, and (iii) concrete carbonation. The proposed coupled water transport and carbonation reactive transport model is combined with a phase field description of cracks and numerically implemented using the finite element method. The proposed theory and details of the finite element implementation are given in Sect. 2. Then, in Sect. 3, model predictions are benchmarked against experimental measurements of relative water mass loss, water saturation ratio, water penetration contours and carbonation penetration depths, for both drying and wetting of cracked and uncracked concrete. In all cases, a very good agreement between simulations and test data is observed. Finally, insight is gained into the role of variable moisture saturation and cracks on the corrosion current density. The manuscript ends with concluding remarks in Sect. 4.

2 Theory and computational implementation

In this section, the underlying theory of the proposed model is presented, together with brief details of the numerical implementation. Firstly, the water transport model resolving water saturation in the concrete pore space is presented in Sect. 2.1. This is followed by the description of the interplay between corrosion current density and water saturation, following the work of [36] (Sect. 2.2). Then, in Sect. 2.3, the concrete carbonation model is provided. Finally, an overview of the governing equations of the model is given in Sect. 2.4.

Notation. Scalar quantities are denoted by light-faced italic letters, e.g. ϕ, Cartesian vectors by upright bold letters, e.g. $\mathbf{u}$, and Cartesian second- and higher-order tensors by bold italic letters, e.g. $\boldsymbol{K}$. The symbol $\mathbf{1}$ represents the second-order identity tensor. Finally, $\boldsymbol{\nabla}$ and $\boldsymbol{\nabla}\cdot$ respectively denote the gradient and divergence operators.

2.1 A model for characterising water transport in cracked concrete

Moisture in concrete can be transported in both liquid and gas form (i.e., as vapour). The analysis of [37] revealed that during the drying of weakly permeable materials such as concrete, the liquid transport mechanism dominates over the contribution of gas transport. In addition, our numerical simulations showed that water vapour transport is also negligible during wetting by liquid water. Accordingly, we proceed to neglect the effects of water vapour transport, evaporation and gas pressure. With these assumptions, following [37], the transport equation of moisture in the concrete domain Ω^c can be formulated as

$$\frac{\partial}{\partial t}\left(\theta \rho_l S_l\right) = -\boldsymbol{\nabla}\cdot\left(\theta S_l \rho_l \mathbf{v}_l\right) \tag{1}$$

where t denotes time, θ is the porosity of concrete, which changes in time with carbonation progress, ρ_l denotes the density of water, S_l is the unknown liquid saturation ratio, and $\mathbf{v}_l$ is the velocity of the liquid phase. Based on Darcy's law [37], the volume flux can be related to the gradient of liquid pressure as

$$\theta S_l \mathbf{v}_l = -\frac{k_r}{\eta}\boldsymbol{K}\cdot\nabla p_l \tag{2}$$

Here, k_r is the relative permeability, η is the dynamic viscosity of liquid water, $\boldsymbol{K}$ is the intrinsic permeability tensor, and p_l is the liquid pressure. The difference between gas pressure p_g and liquid pressure p_l is the capillary pressure $p_c = p_g - p_l$. Since gas pressure is usually negligible, one can assume that $p_l = -p_c$ and, accordingly, Eq. (2) can be expressed in terms of the capillary pressure as

$$\theta S_l \mathbf{v}_l = \frac{k_r}{\eta}\boldsymbol{K}\cdot\nabla p_c \tag{3}$$

The balance equation (1) is written in terms of the liquid saturation ratio S_l as the primary unknown, but the transport law (3) uses the gradient of capillary pressure as the driving force of the transport process. For a given porous material, the capillary pressure p_c can be expressed as a function of the liquid saturation ratio S_l. This function $p_c(S_l)$ is known as the capillary curve and depends on the material. The experimentally determined capillary curve is commonly fitted with the expression originally proposed by Van Genuchten [38], which reads

$$p_c\left(S_l\right) = \alpha\left(S_l^{-\beta} - 1\right)^{1-1/\beta} \tag{4}$$

where α and β are material parameters. It should be noted that if the material undergoes periodic wetting and re-drying, the capillary curve changes because of sorption hysteresis effects. Currently, such effects are not considered in this model, but they could be readily included, as done for example by [39].

Substituting (3) into (1), and assuming incompressibility of water (i.e., constant ρ_l), we obtain

$$\frac{\partial}{\partial t}\left(\theta S_l\right) = -\boldsymbol{\nabla}\cdot\left(\frac{k_r}{\eta}\frac{\mathrm{d}p_c}{\mathrm{d}S_l}\boldsymbol{K}\cdot\nabla S_l\right) \quad \text{in } \Omega^c \tag{5}$$

The capillary pressure is also related to the relative humidity h_r by the Kelvin law, which reads

$$p_c = -\rho_l\frac{RT}{M_l}\ln h_r \tag{6}$$

where R is the gas constant, T is the absolute temperature and M_l is the molar mass of water. The Kelvin law (6) can be used in combination with the capillary curve (4) to calculate the initial condition for S_l and the boundary condition for S_l on surfaces where the relative humidity is known.

By substituting equation (6) into (4), we obtain a relation between relative humidity and saturation ratio that is commonly referred to as a sorption isotherm,

$$S_l(h_r) = \left(1 + \left(-\rho_l\frac{RT}{M_l\alpha}\ln h_r\right)^{\beta/(\beta-1)}\right)^{-1/\beta} \tag{7}$$

The sorption isotherm is calibrated from experimental data by an appropriate choice of parameters α and β. It remains to formulate the expressions for the relative permeability k_r and the intrinsic permeability $\boldsymbol{K}$. The relative permeability k_r determines the ratio of the effective permeability of the liquid water to the total permeability of the porous material. Based on

Mualem's model [40], which predicts hydraulic conductivity from the statistical pore-size distribution, and employing the experimentally-fitted capillary curve (4), [38] derived the following expression for relative permeability k_r:

$$k_r = \sqrt{S_l}\left[1 - \left(1 - S_l^{\beta}\right)^{1/\beta}\right]^2 \tag{8}$$

We proceed now to incorporate the role of cracks. Intrinsic permeability is much higher in cracks than in an undamaged material. Inspired by the phase field hydraulic fracture literature [41–43], we express the intrinsic permeability tensor $\boldsymbol{K}$ as the sum of the contributions of isotropic bulk permeability $\boldsymbol{K}_m$ and an anisotropic cracked permeability $\boldsymbol{K}_c$:

$$\boldsymbol{K} = \boldsymbol{K}_m + \boldsymbol{K}_c \tag{9}$$

The isotropic bulk permeability $\boldsymbol{K}_m$ is here estimated from porosity, following [44];

$$\boldsymbol{K}_m = k\mathbf{1} = \frac{\theta^3}{C\tau^2\rho_s^2}\mathbf{1} \tag{10}$$

where $\mathbf{1}$ is the second-order identity tensor, ρ_s is the density of the dry material and C is a fitting constant. Because tortuosity can be estimated with the Bruggeman relation [44] as $\tau = \theta^{-2.5}$, Eq. (10) can be reformulated as

$$\boldsymbol{K}_m = k\mathbf{1} = \frac{\theta^8}{C\rho_s^2}\mathbf{1} \tag{11}$$

Assuming laminar flow in the crack of opening w, we define the anisotropic cracked permeability $\boldsymbol{K}_c$ as:

$$\boldsymbol{K}_c = \phi\frac{w^2}{12}\left(\mathbf{1} - \mathbf{n}_\phi \otimes \mathbf{n}_\phi\right) \tag{12}$$

where ϕ is a phase field variable characterizing concrete damage [45–49]. Akin to a damage variable, the phase field order parameter changes from $\phi = 0$ in uncracked concrete to $\phi = 1$ in fully cracked material points. The core idea of the phase-field approach is to replace the sharp crack geometry representing a discontinuity in the damage field with the phase-field variable ϕ varying sufficiently smoothly over the crack process zone. In mathematical terms, this is achieved by adding an additional term to the total potential energy density functional which contains $|\nabla\phi|^2$; the reader is referred to (e.g.) Ref. [50, 51] for derivation details. This ensures that large gradients of ϕ are penalised and ϕ is maximal in the centre of the process zone and sufficiently smoothly decreases towards its boundaries. Phase field fracture models have gained increasing attention in recent years and their success has been extended to the modelling of concrete cracking [52–55], including in combination with reactive transport modelling [34, 50, 56–58]. Here, our purpose is to exploit the phase field regularisation of cracks to define regions of initial damage and describe the special characteristics of transport and carbonation within them. Hence, the phase field distribution is given by,

$$\phi + \ell^2\boldsymbol{\nabla}\cdot\nabla\phi = 0 \tag{13}$$

Where ℓ is a phase field length scale that controls the width of the fracture process zone. To achieve mesh-insensitive results, the element size H_e in the process zone must be 5–7 times smaller than ℓ [46]. It remains to define the opening of the crack w. To this end, we define $\mathbf{n}_\phi = \nabla\phi/|\nabla\phi|$ as a normalised vector pointing perpendicularly to the crack, such that the operator $\mathbf{1} - \mathbf{n}_\phi \otimes \mathbf{n}_\phi$ projects the enhancement of permeability only in the direction of the crack. Then, the crack opening w is approximated as

$$w = \begin{cases} 0 \text{ if } \phi < \phi_t \\ w_{cr} \text{ if } \phi \geq \phi_t \end{cases} \tag{14}$$

where w_{cr} is the crack width and ϕ_t is the threshold defining the crack contours as only the part of the regularised phase-field profile represents an opened crack. In the further described case studies, the position of cracks and their widths were known and w_{cr} were thus prescribed directly. However, if cracks result from a coupled mechanical problem, w_{cr} is not known a priori. In such cases, it can be calculated as $w_{cr} = H_e\left(\mathbf{n}_\phi \cdot \boldsymbol{\varepsilon} \cdot \mathbf{n}_\phi\right)$ where $\boldsymbol{\varepsilon} = \nabla_s\mathbf{u}$ is the small strain deformation tensor, with $\mathbf{u}$ being the displacement vector [41, 42].

2.2 Linking the corrosion current density to the water saturation

The water saturation ratio S_l, as determined by Eq. (5), can be related to the corrosion current density, given the dependency of the latter on pore structure and moisture state [36]. The pore structure has a twofold effect. Firstly, it influences the transport of released ferrous

ions into the porosity because the pore structure can act as a diffusion constraint, limiting the corrosion current density. Secondly, together with the moisture state, the pore structure determines the area of the steel surface that is in contact with moisture, which is a necessary condition for the corrosion process to proceed [59, 60]. Based on these ideas, we follow [36] and define the corrosion current density i_c as a function of the water saturation ratio S_l and the material porosity θ, such that

$$i_c = i_{\max}\frac{1}{2}\left(1+\frac{(\theta-\theta_{\text{crit}})}{\sqrt{k+(\theta-\theta_{\text{crit}})^2}}\right)S_l \tag{15}$$

Here, k is a non-dimensional fitting parameter and θ_{crit} is a critical porosity level, with both influencing the shape of the function $i_c(\theta)$. Specifically, θ_{crit} specifies the inflection point of $i_c(\theta)$. The maximum corrosion current density, $i_{\max}$, which depends on the composition of the pore solution, acts as an asymptotic value of (15) and represents the maximum corrosion rate in a completely open system, i.e. solution, without any diffusion constraint by the pore structure. Following the experimental calibration by [36], we adopt $i_{\max} = 3.7\,\mu\text{A/cm}^2$, $k = 10^{-3}$ and $\theta_{\text{crit}} = 0.185$.

2.3 A model for concrete carbonation

The carbonation of Portland cement concrete involves several stages [14, 17]. Firstly, gaseous (g) carbon dioxide present in the air gradually penetrates concrete by means of diffusion through the concrete pore space. The gaseous carbon dioxide then dissolves in concrete pore solution (aq) through the following reactions

$$\begin{aligned}&H_2O + CO_2(g) \rightarrow HCO_3^-(aq) + H^+(aq)\\ &HCO_3^-(aq) \rightarrow CO_3^{2-}(aq) + H^+(aq)\end{aligned} \tag{16}$$

The concrete pore solution also contains calcium cations (Ca^{2+}) emerging from the following dissolution reaction of solid (s) calcium hydroxide ($Ca(OH)_2$) from hardened cement paste

$$Ca(OH)_2(s) \rightarrow Ca^{2+}(aq) + 2OH^-(aq) \tag{17}$$

Then, calcium cations (Ca^{2+}) and carbonate anions (CO_3^{2-}) undergo the following neutralization reaction

$$\begin{aligned}&Ca^{2+}(aq) + 2OH^-(aq) + 2H^+(aq)\\ &\quad + CO_3^{2-}(aq) \rightarrow CaCO_3(s) + 2H_2O\end{aligned} \tag{18}$$

and form calcium carbonate ($CaCO_3$).

Accordingly, the carbonation process of Portland cement has two critical consequences. Firstly, emerging calcium carbonate gradually fills concrete porosity and secondly, calcium hydroxide ($Ca(OH)_2$) is consumed by the carbonation reaction. Because calcium hydroxide is responsible for the basic character of the concrete pore solution (pH 12–13), the carbonation reaction has an acidifying effect, reducing the pH below 9. The acidification of the pore solution prevents the stable preservation of the protective passive layer on the surface, leading to the onset of corrosion [1]. It should be noted that the described series of reactions is valid only for concretes from Portland cement and may differ for blended cement such as blast furnace slag or fly ash cements.

To capture the carbonation process, we enrich our theoretical framework with a carbonation model based on the works by [34] and [17]. To this end, we describe the diffusion of carbon dioxide through a concrete domain Ω^c and the consumption of calcium hydroxide by

$$\frac{\partial}{\partial t}\left(\theta(1-S_l)c_{CO_2}\right) - \boldsymbol{\nabla}\cdot\left(D_{CO_2}\nabla c_{CO_2}\right) = -\theta S_l R_n \quad \text{in } \Omega^c \tag{19}$$

$$\frac{\partial}{\partial t}c_{Ca(OH)_2} = -\theta S_l R_n \quad \text{in } \Omega^c \tag{20}$$

where c_{CO_2} and $c_{Ca(OH)_2}$ are the concentrations of carbon dioxide and calcium hydroxide, respectively. In addition, D_{CO_2} is the diffusivity of carbon dioxide in concrete and R_n is the rate of neutralization reaction (18). The former is calculated as a function of the concrete porosity θ and the water saturation S_l as,

$$D_{CO_2} = 1.64\cdot 10^{-6}\left(\theta+(1-\theta)\phi^{10}\right)^{1.8}(1-S_l)^{2.2} \tag{21}$$

Diffusivity increases with porosity, but the higher the water saturation of pore space, the slower gaseous carbon dioxide can penetrate through concrete. The dependency on the phase field variable ϕ enriches the model to enable capturing the impact of enhanced diffusivity inside of cracks. For uncracked concrete ($\phi = 0$) with 50% saturated porosity ranging between 10–20% of concrete volume, Eq. (21) predicts CO_2 diffusivity levels in the order of magnitude of 10^{-8}

m^2s^{-1}, which agrees with the values measured by [14]. The rate of the neutralization reaction (18) is expressed as

$$R_n = HRTk_n c^{eq}_{OH^-} c_{CO_2} c_{Ca(OH)_2} \tag{22}$$

where H is the Henry constant for the dissolution of CO_2 in water, k_n is the reaction rate constant and $c^{eq}_{OH^-}$ is the OH^- equilibrium concentration.

The progress of the carbonation process is tracked by carbonation front variable $\varphi \in [0, 1]$, which is calculated as

$$\varphi = 1 - \frac{c_{Ca(OH)_2}}{c^0_{Ca(OH)_2}} \tag{23}$$

with $c^0_{Ca(OH)_2}$ being the initial calcium hydroxide concentration. A value of $\varphi = 0$ denotes uncarbonated concrete, while $\varphi = 1$ characterises fully carbonated concrete. The carbonation process affects the porosity of concrete and the pH of the pore solution. These are calculated based on the value of the carbonation front variable φ as

$$\theta = \theta_0 + \varphi(\theta_c - \theta_0); \tag{24}$$

$$\text{pH} = 14 + \log(2 \cdot 10^3 c_{Ca(OH)_2}) \tag{25}$$

In Eq. (24), θ_0 is the initial porosity of uncarbonated concrete and $\theta_c < \theta_0$ is the porosity of fully carbonated concrete. Thus, changes in concrete porosity and pH are naturally captured by predicting the evolution of the concentrations of CO_2 and $Ca(OH)_2$, the primary variables of the carbonation model.

2.4 Overview of the governing equations and details of the numerical implementation

The system of governing equations for the coupled water transport and carbonation problem is given by

$$\frac{\partial}{\partial t}\left(\theta S_l\right) + \boldsymbol{\nabla} \cdot \left(\frac{k_r}{\eta}\frac{\mathrm{d}p_c}{\mathrm{d}S_l}\boldsymbol{K} \cdot \nabla S_l\right) = 0 \quad \text{in } \Omega^c \tag{26a}$$

$$\frac{\partial}{\partial t}\left(\theta\left(1 - S_l\right)c_{CO_2}\right) - \boldsymbol{\nabla} \cdot \left(D_{CO_2} \nabla c_{CO_2}\right) = -\theta S_l R_n \quad \text{in } \Omega^c \tag{26b}$$

$$\frac{\partial}{\partial t} c_{Ca(OH)_2} = -\theta S_l R_n \quad \text{in } \Omega^c \tag{26c}$$

With the primary unknowns being the water saturation ratio in the pore space S_l, the concentration of carbon dioxide c_{CO_2} and the concentration of calcium hydroxide $c_{Ca(OH)_2}$. Dirichlet boundary conditions are prescribed on the boundaries of concrete exposed to atmospheric conditions (air or water); i.e. $S_l = \bar{s}$ and $c_{CO_2} = \bar{c}$, while on protected boundaries zero flux of water or carbon dioxide is considered (i.e. $\mathbf{n} \cdot \boldsymbol{K} \cdot \nabla S_l = 0$ and $\mathbf{n} \cdot D_{CO_2} \nabla c_{CO_2} = 0$). Equation (26c) does not contain any space derivatives and thus does not require any boundary conditions. The numerical implementation is carried out using the finite element method and the system of differential equations (26a)–(26c) is solved using a fully implicit solution scheme. The concrete domain Ω^c is discretised with linear quadrilateral elements. All numerical simulations are performed using the open-source computing platform DEAL.II [61, 62].

3 Results

We proceed to showcase the ability of the model to predict experiments and provide new insight. To ensure consistency, a set of material parameters are first defined in Sect. 3.1, which are subsequently used to predict the outcome of independent experiments with different boundary conditions. Specifically, the ability to replicate water transport during wetting and drying in uncracked concrete is validated with the experiments by [63] and [44] in Sects. 3.2 and 3.3, respectively. The ability of the model to capture the impact that cracks have on water transport is evaluated in Sect. 3.4, by benchmarking model predictions against the experimental data of [64]. In Sect. 3.5, the coupling between water transport and carbonation is assessed by comparing predictions of carbonation depth under variable humidity with the testing data of [65]. Finally, in Sect. 3.6, the validated model is used to gain new insight into the evolution of carbonation and induced corrosion current density in cracked and uncracked samples subjected to cyclic wetting and drying.

3.1 Choice of model parameters

For consistency, the same set of concrete material parameters is used across all numerical experiments. The parameters describing water and carbon dioxide

transport in concrete are taken from the experimental literature and listed in Table 1.

Some parameters deserve detailed consideration. In the proposed model, the water permeability of uncracked concrete $\boldsymbol{K}_m$ is not constant in time but rather evolves with the changing porosity of concrete caused by carbonation. For this reason, it is important to accurately determine the magnitude of parameter C, which links water permeability and porosity, see Eq. (11). Here, $C = 7.4 \cdot 10^6$ m^4 kg^{-2} is adopted for the drying process, which leads to permeability values in the order of magnitude of 10^{-21} m^2, as reported by [37]. The value of $C = 1.29 \cdot 10^2$ m^4 kg^{-2} is adopted for the wetting process, as it leads to permeability values in the order of magnitude of 10^{-16} m^2, as measured by [44]. Thus, water permeability values employed in case studies 1 (Sect. 3.2) and 2 (Sect. 3.3) are consistent with experimentally measured permeabilities reported in their respective studies. Let us note here that [66] analysed experimentally measured permeability of cementitious materials reported in the literature and concluded that water permeability is on the order of 10^{-21} m^2 for both pastes or concretes with w/c between 0.4 and 0.5 made from Portland cement. While a permeability reported by [37] (w/c = 0.48, Portland cement) matches this conclusion perfectly, we can see that the permeability recovered by [66] is several orders of magnitude larger. Although the samples of [66] had different composition (w/c = 0.6, blended cement containing burnt oil shale and limestone), [66] concluded that this discrepancy likely results primarily from the carbonation-induced coarsening of pores. Regarding case study 3 (Sect. 3.4), [64] did not experimentally investigate the permeability of his cracked concrete samples (w/c = 0.5, Portland cement) and thus for this study, it was roughly estimated to be the same as in case study 2 (Sect. 3.3). An excellent match of numerically predicted and experimentally measured extent of water distribution in time suggests that the choice of permeability is appropriate.

The sorption isotherm constants were experimentally calibrated following the studies by [37] and [44] for drying and wetting conditions, respectively. It is worth noting that the authors of these studies recovered α and β from experimental data on different concrete samples. This results in both curves crossing at approximately 20% relative humidity which would theoretically not be expected. Figure 1 shows the differences between the sorption isotherm for wetting and its counterpart for drying. Again, values numerically employed in case studies 1 (Sect. 3.2) and 2 (Sect. 3.3) are consistent with experimentally recovered sorption isotherm constants in these studies. For the sake of the applicability of these values, it is important to mention that [44] notes that because the equilibrium water content in a cementitious material is mainly controlled by the amount of dry-hardened cement paste, it can be expected that cementitious materials with the same type of cement and w/c ratio have a very similar sorption isotherm. In the case study 3 (Sect. 3.4), [64] did not experimentally measure sorption isotherm. For this reason, the same values of the wetting isotherm constants were used as in case study 2 (Sect. 3.3). While this constitutes an approximation, a parameter sensitivity study reveals only a small influence on the numerical results, with the influence being only noticeable in the water distribution at the very early stages.

Let us also reiterate that the chosen carbonation model and values of its parameters are aimed at modelling Portland cement-based materials. Although the samples of [65] (w/c = 0.55) considered in case study 4 (Sect. 3.5) contained fly ash in addition to Portland cement, an excellent fit of predicted and experimentally measured carbonation penetration suggests that the choice of material parameters is appropriate in this case too.

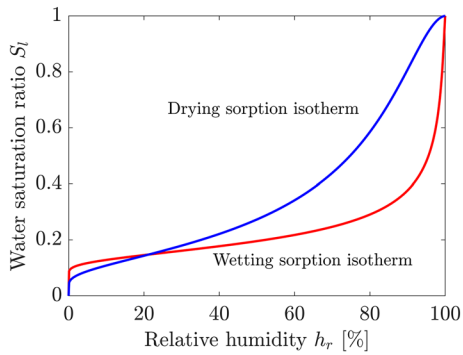

Fig. 1 The comparison of wetting and drying sorption isotherm. Curves estimated using Eq. (7) with the experimentally-calibrated values of α and β given in Table 1

Table 1 Model parameters for describing water and carbon dioxide transport in concrete

Parameter	Value	Unit	Source
CO_2 *transport*			
Henry constant H for CO_2 dissolution in water	$3.375 \cdot 10^{-4}$	mol Pa^{-1} m^{-3}	[14]
Neutralization reaction constant k_n	8.3	m^3 mol^{-1} s^{-1}	[14]
OH^- equilibrium concentration $c^{eq}_{OH^-}$	43.2	mol m^{-3}	[14]
Initial $Ca(OH)_2$ concentration $c^0_{Ca(OH)_2}$	$1.2 \cdot 10^{-4}$	mol m^{-3}	[17]
Porosity of fully carbonated concrete θ_c	0.11	–	[24]
Water transport			
Concrete water permeability constant C (wetting and drying)	$1.29 \cdot 10^2$ & $7.4 \cdot 10^6$	m^4 kg^{-2}	[37, 44]
Dynamic viscosity of water η	10^{-3}	Pa·s	[43]
Phase-field threshold ϕ_t	0.5	–	[43]
Density of dried concrete ρ_s	2285	kg m^{-3}	[37]
Sorption isotherm parameter α (wetting and drying)	$0.9 \cdot 10^6$ & $18.62 \cdot 10^6$	Pa	[37, 44]
Sorption isotherm parameter β (wetting and drying)	3.85 & 2.27	–	[37, 44]
Saturation-dependent corrosion current density model			
Maximum effective current density i_{max}	3.7	$\mu A/cm^2$	[36]
Constant k	10^{-3}	–	[36]
Critical porosity θ_{crit}	0.185	–	[36]

3.2 Case study 1: Drying of uncracked concrete

The ability of the model to predict water transport under drying conditions is evaluated by simulating the experimental tests by [63]. Their experiments were based on two-year-old cylindrical cement paste samples with 160 mm diameter and 100 mm height, as shown in the cross-section geometry provided in Fig. 2a. Moisture exchange was allowed only on the flat base boundaries while it was prevented on the the curved boundary. During the drying process, the external relative humidity was 50% and the temperature was 20°C. Initial relative humidity before drying was measured to be 87%. Because the distribution of initial relative humidity was reported to be uniform, the drying test was simulated as a one-dimensional problem. The porosity of the sample, as measured by [63], was $\theta = 0.12$. The relevant experimental outcome reported by [63] is the relative water mass loss, which is numerically estimated as

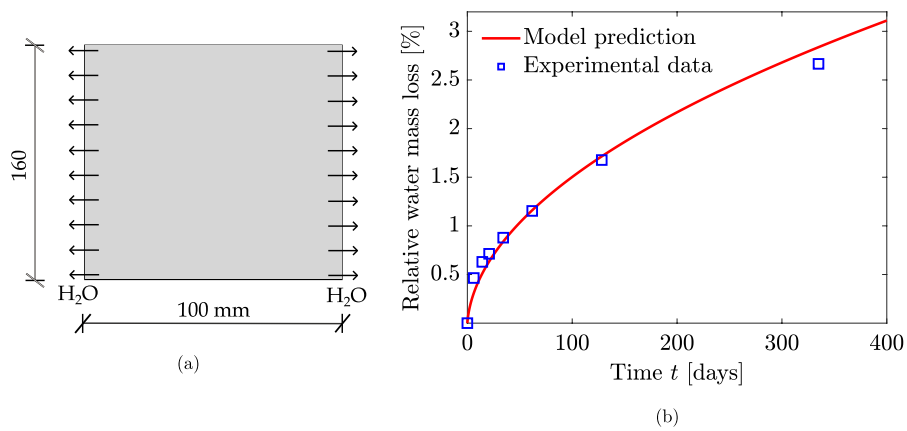

Fig. 2 Simulation of the drying test of [63]: **a** geometry of the cross-section of the cylindrical cement paste specimen, and **b** comparison of predicted and experimentally measured water mass loss in time (expressed in percents of the original water mass content)

$$\Delta w_r(t) = 100 \int_{\Omega_c} \frac{S_l(0) - S_l(t)}{S_l(0)} \, \mathrm{d}V \tag{27}$$

The predicted water mass loss as a function of time is given in Fig. 2b, together with the experimental results. A very good agreement between model predictions and experiments is observed.

3.3 Case study 2: Wetting of uncracked concrete

We proceed now to examine the model's capabilities in predicting water transport under wetting conditions. To this end, numerical predictions are compared against the experimental results by [44]. Zhang et al. [44] conducted experiments on a 3 mm thick, 32 mm × 2 mm rectangular mortar sample with two embedded steel wires (see Fig. 3a), which was placed on top of a distilled water reservoir such that the lower surface was permanently wetted. Water evaporation from both front and back surfaces was prevented by covering them with aluminium adhesive sheets. Before the wetting test, specimens were carbonated and then stored for seven days in an environment of 53% relative humidity. Water saturation on the surface of the upper steel wire was monitored during the wetting test. Mortar porosity was measured to be about $\theta = 0.15$ but was reported to increase significantly in the close vicinity of the steel wires. Thus, as suggested by [44], a highly porous layer of 0.3 mm is considered, where porosity changes linearly between 15 and 70% (see Fig. 3a). The simulation and experimental results are given in Fig. 3b. A very good level of agreement is obtained across the whole time spectrum, with only small differences being observed around the 30–35 min interval, where the scatter in the experimental data appears to be the largest.

3.4 Case study 3: Wetting of cracked concrete

The presence of cracks significantly affects water transport. To validate the ability of the model to accurately capture the enhancement of water transport through cracks, we choose to model the experiments by [64].

Michel and Pease [64] used non-destructive X-ray attenuation to monitor the evolution of water saturation in samples containing a single crack. Specifically, as shown in Fig. 4, they employed two-year-old 100 × 100 mm rectangular samples with a thickness of 50 mm. The sample porosity was estimated from the maximum measured water saturation and reported to be equal to $\theta = 0.12$. Michel and Pease [64] introduced cracks into the notched samples by means of a splitting load, which was applied via a rigid wedge using crack mouth opening displacement (CMOD) control. All specimens were conditioned at 50% relative humidity and a temperature of 20°C for at least 1 year before wetting. The simulated part of the domain with the crack is depicted in Fig. 4. The crack was measured

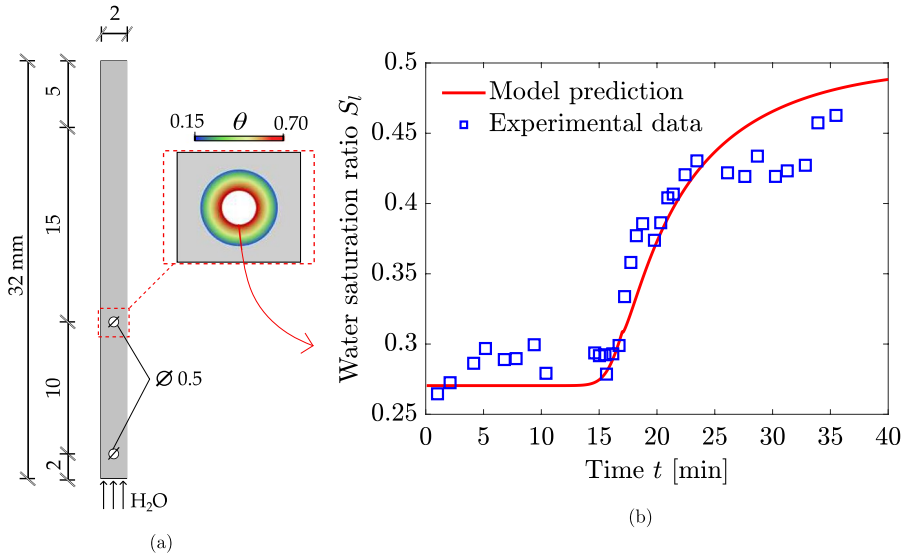

Fig. 3 Simulation of the wetting test of [44]: **a** Geometry of the cross-section of the mortar specimen with two embedded steel wires, with the inset figure showcasing how the gradual change in porosity reported by [44] is accounted for; and **b** comparison of the evolution of the predicted and experimentally measured water saturation ratios in the vicinity of the upper steel wire

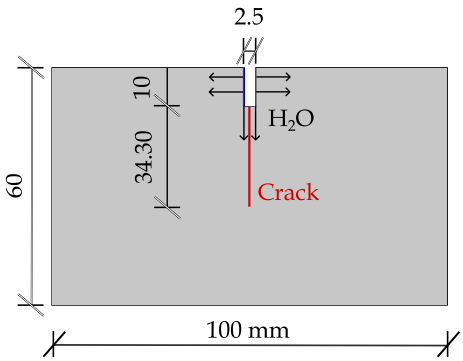

Fig. 4 Simulation of the wetting test of [64]—cross-section of the concrete samples containing a single crack

to be 34.3 mm long and 0.043 mm wide, with the crack opening decreasing with depth, as reported by [64]. Accordingly, we introduce the crack into the model by assigning $\phi = 1$ in the centre of the crack and smearing the cracked domain using Eq. (13). The choice of $\ell = 0.043$ mm leads to the experimentally reported opening of the crack on the surface such that $\phi \geq \phi_t$ on the region of the same width. During the wetting test, a cast-in recess and a cut notch above the crack were used as a reservoir of liquid water. For this reason, $S_l = 1$ was considered on the boundaries of the notch. On the top surface of the specimen, water saturation equivalent to 65% relative humidity is considered, as these are the conditions relevant to the X-ray chamber. Mimicking the experimental setup, we consider zero flux on the remaining concrete surfaces. In Fig. 5, the experimentally measured envelope of a partially water-saturated region is compared with the predicted distribution of water saturation at different times, up to seven hours from the beginning of the wetting process.

The notable impact of cracks in water transport is evident from the very early stages of the test, see Fig. 5a ($t = 0.03$ h). Water transport is significantly enhanced in the vertical direction, particularly at the beginning of the experiment. With time, the water distribution is more uniform and the contour shows a semi-ellipsoidal shape, with both axes of the ellipse expanding in time. For all the evaluated times, the extent of water distribution agrees with their experimental counterparts very well, indicating that the model is able to accurately predict water transport in cracked concrete samples undergoing wetting.

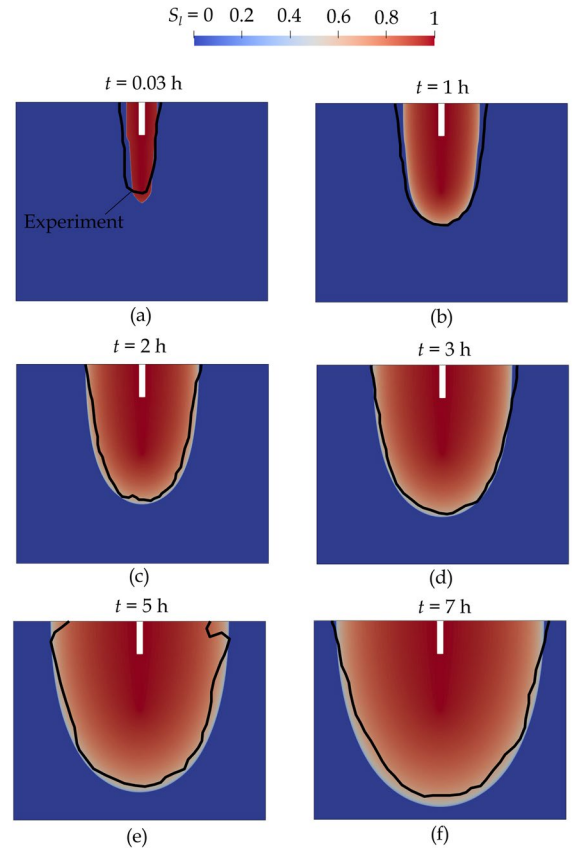

Fig. 5 Simulation of the wetting tests of [64] of concrete samples with a single crack. Contours of simulated saturation ratio and experimentally measured envelope of water distribution (black line) after a time of **a** 0.03 h, **b** 1 h, **c** 2 h, **d** 3 h, **e** 5 h, and **f** 7 h

3.5 Case study 4: Carbonation of variably water-saturated concrete

We shall now use the carbonation depth measurements by [65] to investigate the ability of the model to capture the interplay between carbonation and water saturation. [65] conducted experiments on concrete cubes of characteristic length 100 mm that had been cured for 28 days and subsequently dried for 2 days at 60°C, so as to minimise the presence of water. The initial porosity is deemed to be $\theta_0 = 0.26$, based on the model of [67] for a reported water-cement ratio of 0.55 and assuming a degree of hydration of 0.9. As sketched in Fig. 6a, the experiments involved using an environmental chamber to expose two opposite sides of the sample to a constant temperature of 19.85°C and a fixed carbon dioxide concentration of 20% CO_2.

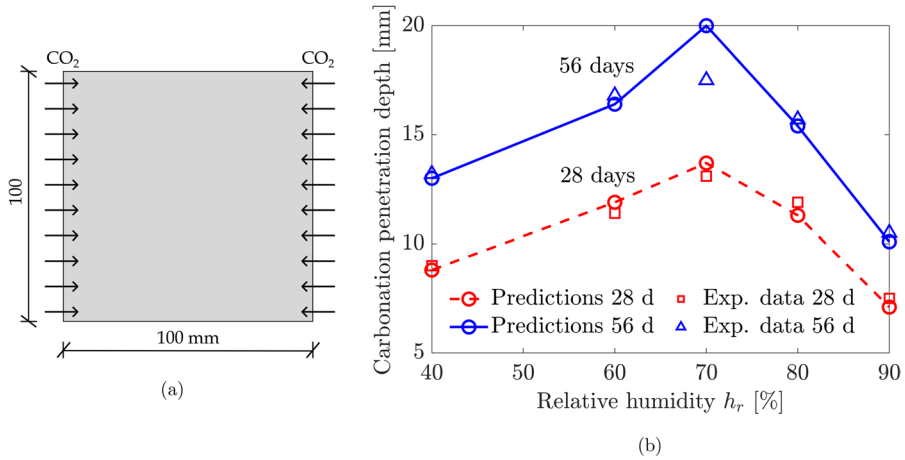

Fig. 6 Simulation of the carbonation tests of [65]: **a** Geometry of the cross-section of the concrete specimen, and **b** comparison of predicted and experimentally measured carbonation depth for varying relative humidity. The proposed model accurately predicts the concave dependency of the carbonation depth on the relative humidity. This results from the competition between CO_2 diffusivity decreasing with increasing water saturation and the reaction rate of neutralization reaction increasing with increasing water saturation

In contrast, the relative humidity was varied from 40 to 90%, so as to estimate carbon penetration depths as a function of time and relative humidity h_r. As shown in Fig. 6b, measurements were taken after 28 and 56 days of exposure.

Model predictions are also shown in Fig. 6b, using circle symbols and lines. Numerical predictions for both 28 and 56 days agree with experimental measurements very well. Only for the case of 70% relative humidity and 56 days, the model overestimates the carbonation depth, by approximately 2 mm. In Fig. 6b we can see that the curve depicting the dependence of carbonation depth on relative humidity is concave. This is caused by two competing effects arising with increasing water saturation—an increase of the reaction rate of the neutralization reaction, see Eq. (19), and a decrease of carbon dioxide diffusivity, see Eq. (21). If water saturation is low, gaseous carbon dioxide penetrates the concrete pore space easily, but the carbonation reaction takes place in pore solution and is thus hindered by low water content. On the other hand, if water saturation of pore space is high, carbonation proceeds quickly but the transport of carbon dioxide is significantly hindered. As shown in Fig. 6b, this leads to the existence of an optimal water saturation point under which the quickest carbonation rate is observed. For the described tests of [65], the maximum carbonation depth was observed for a 70% relative humidity, and this is also the case in our simulations.

3.6 Case study 5: Insights into the interplay between carbonation, cyclic wetting/drying and corrosion

During the carbonation process, exposed reinforced concrete structures are subjected to cyclic wetting and drying. Because the carbonation rate is highly dependent on the water saturation of concrete pores, as showcased in the previous section, the time to steel depassivation is also sensitive to these humidity changes. Also, changes in water saturation lead to changes in corrosion current density (see Sect. 2.2). Cracks resulting from loading, temperature gradients, shrinkage and other effects are commonly present in reinforced concrete structures and significantly enhance the transport of water and carbon dioxide, accelerating carbonation. To demonstrate how the proposed model can be used to investigate the interaction of these processes during alternating wetting and drying, the behaviour of a 50 mm × 50 mm concrete sample reinforced with a single rebar of 16 mm diameter is investigated (see Fig. 8a, b). A 16% porosity was considered. Penetration of water and carbon dioxide was allowed on two perpendicular surfaces while zero flux for both species was considered on the two remaining surfaces. The specimen had an initial

pore water saturation of 40% and the saturation of exposed boundaries changed periodically from 40 to 80%. The exposed boundary saturation varied in time as $S_l = 0.4(1 + 0.5(\sin(\pi t/7 + 1.5\pi) + 1))$ and the cycle time was thus 14 days. For the sake of simplicity, only the wetting isotherm is employed. To investigate the effect of cracks, both uncracked (Fig. 8a) and cracked (Fig. 8b) samples are considered. The cracked sample contains two 15 mm long cracks, which start from each of the exposed surfaces. These cracks were numerically introduced by prescribing $\phi = 1$ in the centre of the crack and then regularised using Eq. (13) and adopting a phase field length scale of $\ell = 0.5$ mm.

Contours of the carbonation front variable are shown in Fig. 8a–c for selected concrete water saturation levels after 120 days of exposure. The results obtained for constant water saturation values of 40% and 80% are given in Fig. 8a and b, respectively. It is useful to compare them with the results obtained for variable exposed boundary water saturation, Fig. 8c. While constant 40% water saturation leads to the slowest advance of carbonation front, in agreement with expectations, periodic wetting and drying between 40% and 80% leads to nearly the same result as a constant 80% saturation. This is because periodic wetting events are able to sustain high water saturation which allows for the quicker advance of the carbonation front. Thus, our results highlight how short wetting events can have a profound impact on the long-term water saturation of concrete. This was documented for example by [68], who found out that rain periods are the main factor influencing the internal relative humidity of unsheltered concrete samples. For this reason, even short cyclic periods of high external humidity seem to potentially lead to nearly the same rebar depassivation as if the maximum of periodic boundary saturation remained on the whole domain during the entire time period. Also, it has been observed that the average corrosion current density in samples subjected to cyclic wetting and drying could be comparable to permanently wet samples [69].

The combined effect of variable moisture saturation and cracks on the variation of the corrosion current density is shown in Fig. 8d. As it can be observed, the corrosion current density (evaluated at point A, see Fig. 7), exhibits significant sensitivity to water concentration, varying between 0.28 and 0.56 μA/cm^2. This finding emphasises the need to account for the role of water saturation on carbonation-induced corrosion current density. Also, it can be observed that the presence of cracks significantly

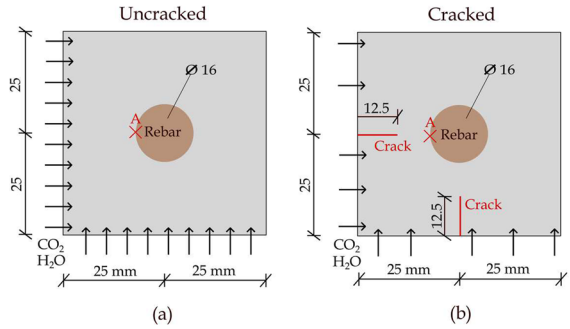

Fig. 7 Geometry of the cross-section of reinforced concrete samples subjected to carbon dioxide penetration and cyclic wetting and drying: **a** uncracked sample and **b** cracked sample. Point A marks the location where the corrosion current density is evaluated

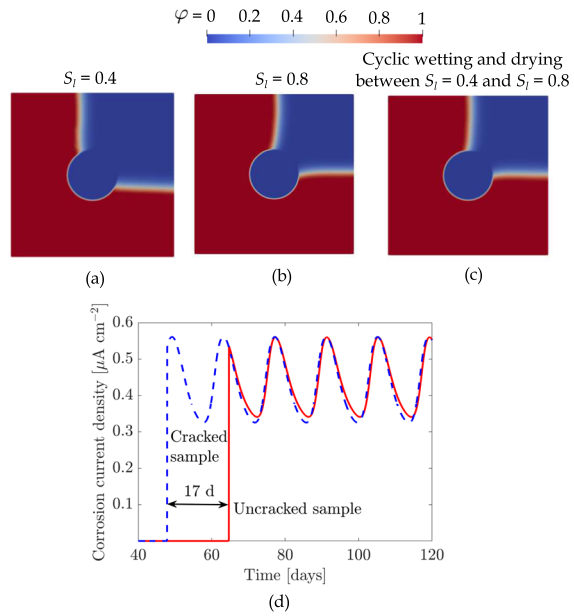

Fig. 8 Carbonation front after 120 days for an uncracked concrete sample subjected to **a** constant 40% water saturation of concrete pore space, **b** constant 80% water saturation, and **c** initial 40% water saturation followed by cyclic 40–80% water saturation of the exposed boundaries. In **d**, the evolution of corrosion current density under cyclic water saturation at point A (see Fig. 7) is compared for cracked and uncracked samples

shortens the time to corrosion initiation, going from approximately 65 to 48 days. Thus, durability models neglecting the role of cracks in enhancing transport and corrosion should be revisited.

4 Conclusions

In this study, we have presented a novel coupled model for water transport, carbonation and corrosion in concrete. Additionally, the new formulation presented can capture the role of cracks in enhancing water and CO_2 transport. The proposed model was extensively validated against experimental data for wetting [44] and drying [63] of uncracked concrete, wetting of cracked concrete [64], and carbonation under varying water saturation [65]. Although all these studies considered different concrete samples, their main difference from the water transport and carbonation perspective lies in the porosity of cement paste and the structure of pore space. Porosity is the principal variable of the model and when set according to measured data or estimated when no measurements were available, the model proved to be able to replicate experimentally measured results from [44, 63–65] very well. However, let us note here that carbonation was found to affect the structure of pore space [44] and although data from this study allowed for the validation of the wetting of uncracked carbonated concrete, other water transport regimes such as drying or wetting of cracked concrete were possible to validate only with uncarbonated samples because of the lack of available experimental data. If such data will become available in the future, we recommend repeated model validation. Furthermore, we build upon the abilities of the model to gain insight into the interplay between corrosion, cracks, and water and CO_2 transport under cyclic wetting and drying conditions. Key findings include:

- The model can accurately simulate the wetting and drying of concrete under isothermal conditions, including the enhancement of water transport through cracks.
- The model is able to accurately capture the impact of water saturation on carbonation, including the interplay between the opposite trends of saturation-dependent neutralization reaction rate and saturation-dependent carbon dioxide diffusivity. An optimal water saturation point is identified for an intermediate value of humidity.
- Cyclic wetting and drying leads to significant acceleration in the evolution of the carbonation front. Because the drying process tends to be much slower than wetting, even a short intense wetting period can significantly accelerate the carbonation process.
- The corrosion current density changes significantly with varying concrete saturation such that for a concrete specimen with boundary water saturation periodically varying between 40 and 80%, the corrosion current density periodically drops to 56% of its maximum value.
- The time to corrosion initiation is significantly shortened if surface cracks are present, a 30% reduction is observed in the investigated case study.

The model can readily be extended to account for the role of: (i) growing cracks, e.g. by incorporating a phase field evolution law [34, 50], (ii) sorption hysteresis effects, e.g., as in [39], (iii) chloride-induced corrosion, to capture the interplay between carbonation- and chloride-driven corrosion processes [29], (iv) types of wetting cycles, and (v) the role of oxygen saturation, of potentially high importance yet still not completely understood [36, 70, 71].

Acknowledgements The authors would like to express their gratitude to Prof Milan Jirásek (Czech Technical University in Prague) for his invaluable advice on the formulation of the water transport model and to Prof Hong S. Wong (Imperial College London) for stimulating discussions. E. Korec acknowledges financial support from the Imperial College President's PhD Scholarships. E. Martínez-Pañeda was supported by a UKRI Future Leaders Fellowship [grant MR/V024124/1]. F. Freddi and L. Mingazzi were supported by the Project ECOSISTER SPOKE 4 funded under the National Recovery and Resilience Plan (NRRP), Mission 04 Component 2 Investment 1.5 - NextGenerationEU, Call for tender n. 3277 dated 30/12/2021.

References

1. Poursaee A, Lasa I, Hansson C, McDonald D, Yeomans S, Holland R, Kurtis K, Kahn L, Moriconi G, Ziehl P, ElBatanouny M, Burkan Isgor O, Andrade C, Spragg R, Qiao C, Weiss J (2016) Corrosion of steel in concrete structures. In: Poursaee A (ed) Corrosion of steel in concrete structures. Woodhead Publishing, Oxford, pp 19–33
2. Angst UM (2018) Challenges and opportunities in corrosion of steel in concrete. Mater Struct 51:1–20
3. Andrade C (2019) Propagation of reinforcement corrosion: principles, testing and modelling. Mater Struct 52:1–26
4. Gehlen C, Andrade C, Bartholomew M, Cairns J, Gulikers J, Javier Leon F, Matthews S, McKenna P, Osterminski K, Paeglitis A, Straub D (2011) Fib Bulletin 59—Condition control and assessment of reinforced concrete structures exposed to corrosive environments (carbonation/chlorides), fib—the international federation for structural concrete
5. Jones AEK, Marsh BK (1997) Development of an holistic approach to ensure the durability of new concrete construction. British Cement Association (BCA)
6. Angst U, Moro F, Geiker M, Kessler S, Beushausen H, Andrade C, Lahdensivu J, Köliö A, Imamoto KI, von Greve-Dierfeld S, Serdar M (2020) Corrosion of steel in carbonated concrete: mechanisms, practical experience, and research priorities—a critical review by RILEM TC 281-CCC. RILEM Tech Lett 5:85–100
7. Yang S, Yang Y, Caggiano A, Ukrainczyk N, Koenders E (2022) A phase-field approach for portlandite carbonation and application to self-healing cementitious materials. Mater Struct 55:1–19
8. Zhang S, Ghouleh Z, Azar A, Shao Y (2021) Improving concrete resistance to low temperature sulfate attack through carbonation curing. Mater Struct 54:1–18
9. Dhandapani Y, Joseph S, Bishnoi S, Kunther W, Kanavaris F, Kim T, Irassar E, Castel A, Zunino F, Machner A, Talakokula V, Thienel KC, Wilson W, Elsen J, Martirena F, Santhanam M (2022) Durability performance of binary and ternary blended cementitious systems with calcined clay: a RILEM TC 282 CCL review. Mater Struct 55:145
10. von Greve-Dierfeld S, Lothenbach B, Vollpracht A, Wu B, Huet B, Andrade C, Medina C, Thiel C, Gruyaert E, Vanoutrive H, Saéz del Bosque IF, Ignjatovic I, Elsen J, Provis JL, Scrivener K, Thienel KC, Sideris K, Zajac M, Alderete N, Cizer Ö, Van den Heede P, Hooton RD, Kamali-Bernard S, Bernal SA, Zhao Z, Shi Z, De Belie N (2020) Understanding the carbonation of concrete with supplementary cementitious materials: a critical review by RILEM TC 281-CCC. Mater Struct 53:136
11. Leemann A, Pahlke H, Loser R, Winnefeld F (2018) Carbonation resistance of mortar produced with alternative cements. Mater Struct 51:1–12
12. Leemann A, Nygaard P, Kaufmann J, Loser R (2015) Relation between carbonation resistance, mix design and exposure of mortar and concrete. Cement Concr Compos 62:33–43
13. Auroy M, Poyet S, Le Bescop P, Torrenti JM, Charpentier T, Moskura M, Bourbon X (2015) Impact of carbonation on unsaturated water transport properties of cement-based materials. Cem Concr Res 74:44–58
14. Papadakis VG, Vayenas CG, Fardis MN (1991) Fundamental modeling and experimental investigation of concrete carbonation. ACI Mater J 88:363–373
15. Saetta AV, Schrefler BA, Vitaliani RV (1993) The carbonation of concrete and the mechanism of moisture, heat and carbon dioxide flow through porous materials. Cem Concr Res 23:761–772
16. Steffens A, Dinkler D, Ahrens H (2002) Modeling carbonation for corrosion risk prediction of concrete structures. Cem Concr Res 32:935–941
17. Isgor OB, Razaqpur AG (2004) Finite element modeling of coupled heat transfer, moisture transport and carbonation processes in concrete structures. Cement Concr Compos 26:57–73
18. Song HW, Kwon SJ, Byun KJ, Park CK (2006) Predicting carbonation in early-aged cracked concrete. Cem Concr Res 36:979–989
19. Bary B, Sellier A (2004) Coupled moisture—carbon dioxide-calcium transfer model for carbonation of concrete. Cem Concr Res 34:1859–1872
20. Omikrine-Metalssi O, Aït-Mokhtar A, Turcry P (2020) A proposed modelling of coupling carbonation-porosity-moisture transfer in concrete based on mass balance equilibrium. Constr Build Mater 230:116997
21. Hwang JY, Kwak HG, Shim M (2020) Numerical approach for concrete carbonation considering moisture diffusion. Mater Struct 53:1–10
22. Seigneur N, Kangni-Foli E, Lagneau V, Dauzères A, Poyet S, Bescop PL, L'Hôpital E, d'Espinose de Lacaillerie JB (2020) Predicting the atmospheric carbonation of cementitious materials using fully coupled two-phase reactive transport modelling. Cem Concr Res 130:105966
23. Seigneur N, De Windt L, Poyet S, Socié A, Dauzères A (2022) Modelling of the evolving contributions of gas transport, cracks and chemical kinetics during atmospheric carbonation of hydrated C3S and C-S-H pastes. Cem Concr Res 160:106906
24. Bretti G, Ceseri M, Natalini R, Ciacchella MC, Santarelli ML, Tiracorrendo G (2022) A forecasting model for the porosity variation during the carbonation process. GEM Int J Geomath 13:1–24
25. Nguyen TT, Bary B, De Larrard T (2015) Coupled carbonation-rust formation-damage modeling and simulation of steel corrosion in 3D mesoscale reinforced concrete. Cem Concr Res 74:95–107
26. Forsdyke JC, Lees JM (2023) Model fitting to concrete carbonation data with non-zero initial carbonation depth. Mater Struct 56:1–11
27. Phung QT, Maes N, Jacques D, De Schutter G, Ye G, Perko J (2016) Modelling the carbonation of cement

pastes under a CO2 pressure gradient considering both diffusive and convective transport. Constr Build Mater 114:333–351
28. Kari OP, Puttonen J, Skantz E (2014) Reactive transport modelling of long-term carbonation. Cement Concr Compos 52:42–53
29. Zhu X, Zi G, Cao Z, Cheng X (2016) Combined effect of carbonation and chloride ingress in concrete. Constr Build Mater 110:369–380
30. Shen XH, Jiang WQ, Hou D, Hu Z, Yang J, Liu Q (2019) Numerical study of carbonation and its effect on chloride binding in concrete. Cement Concrete Composit 104:103402
31. Meijers SJ, Bijen JM, De Borst R, Fraaij AL (2005) Computational results of a model for chloride ingress in concrete including convection, drying-wetting cycles and carbonation. Mater Struct 38:145–154
32. Li K, Zhang Y, Wang S, Zeng J (2018) Impact of carbonation on the chloride diffusivity in concrete: experiment, analysis and application. Mater Struct 51:1–15
33. Xie M, Dangla P, Li K (2021) Reactive transport modelling of concrete subject to de-icing salts and atmospheric carbonation. Mater Struct 54:1–15
34. Freddi F, Mingazzi L (2022) A predictive phase-field approach for cover cracking in corroded concrete elements. Theoret Appl Fract Mech 122:103657
35. Grassl P (2009) A lattice approach to model flow in cracked concrete. Cement Concr Compos 31:454–460
36. Stefanoni M, Angst UM, Elsener B (2019) Kinetics of electrochemical dissolution of metals in porous media. Nat Mater 18:942–947
37. Mainguy M, Coussy O, Baroghel-Bouny V (2001) Role of air pressure in drying of weakly permeable materials. J Eng Mech 127:582–592
38. Van Genuchten MT (1980) A closed-form equation for predicting the hydraulic conductivity of unsaturated soils. Soil Sci Soc Am J 44:892–898
39. Zhang Z, Thiery M, Baroghel-Bouny V (2015) Numerical modelling of moisture transfers with hysteresis within cementitious materials: Verification and investigation of the effects of repeated wetting-drying boundary conditions. Cem Concr Res 68:10–23
40. Mualem Y (1976) A new model for predicting the hydraulic conductivity of unsaturated porous media. Water Resour Res 12:513–522
41. Miehe C, Mauthe S, Teichtmeister S (2015) Minimization principles for the coupled problem of Darcy-Biot-type fluid transport in porous media linked to phase field modeling of fracture. J Mech Phys Solids 82:186–217
42. Wilson ZA, Landis CM (2016) Phase-field modeling of hydraulic fracture. J Mech Phys Solids 96:264–290
43. Heider Y, Sun WC (2020) A phase field framework for capillary-induced fracture in unsaturated porous media: drying-induced vs hydraulic cracking. Comput Methods Appl Mech Eng 359:112647
44. Zhang Z, Trtik P, Ren F, Schmid T, Dreimol CH, Angst U (2022) Dynamic effect of water penetration on steel corrosion in carbonated mortar: a neutron imaging, electrochemical, and modeling study. Cement 9:100043
45. Wu J-Y, Chen WX (2021) Phase-field modeling of electromechanical fracture in piezoelectric solids: analytical results and numerical simulations. Comput Methods Appl Mech Eng 387:114125
46. Kristensen PK, Niordson CF, Martínez-Pañeda E (2021) An assessment of phase field fracture: crack initiation and growth. Philos Trans R Soc A Math Phys Eng Sci 379:20210021
47. Miehe C, Welschinger F, Hofacker M (2010) Thermodynamically consistent phase-field models of fracture: variational principles and multi-field FE implementations. Int J Numer Meth Eng 83:1273–1311
48. Amor H, Marigo JJ, Maurini C (2009) Regularized formulation of the variational brittle fracture with unilateral contact: numerical experiments. J Mech Phys Solids 57:1209–1229
49. Bourdin B, Francfort GA, Marigo JJ (2000) Numerical experiments in revisited brittle fracture. J Mech Phys Solids 48:797–826
50. Korec E, Jirásek M, Wong HS, Martínez-Pañeda E (2023) A phase-field chemo-mechanical model for corrosion-induced cracking in reinforced concrete. Constr Build Mater 393:131964
51. Carrara P, Ambati M, Alessi R, De Lorenzis L (2020) A framework to model the fatigue behavior of brittle materials based on a variational phase-field approach. Comput Methods Appl Mech Eng 361:112731
52. Navidtehrani Y, Betegón C, Martínez-Pañeda E (2022) A general framework for decomposing the phase field fracture driving force, particularised to a Drucker–Prager failure surface. Theoret Appl Fract Mech 121:103555
53. Huang Y, Yang Z, Zhang H, Natarajan S (2022) A phase-field cohesive zone model integrated with cell-based smoothed finite element method for quasi-brittle fracture simulations of concrete at mesoscale. Comput Methods Appl Mech Eng 396:115074
54. Wu J-Y (2017) A unified phase-field theory for the mechanics of damage and quasi-brittle failure. J Mech Phys Solids 103:72–99
55. Wu J-Y (2018) Robust numerical implementation of non-standard phase-field damage models for failure in solids. Comput Methods Appl Mech Eng 340:767–797
56. Pundir M, Kammer DS, Angst U (2023) Journal of the Mechanics and Physics of Solids An FFT-based framework for predicting corrosion-driven damage in fractal porous media. J Mech Phys Solids 179:105388
57. Wu J-Y, Chen WX (2022) On the phase-field modeling of fully coupled chemo-mechanical deterioration and fracture in calcium leached cementitious solids. Int J Solids Struct 238:111380
58. Korec E, Jirásek M, Wong HS, Martínez-Pañeda E (2024) Phase-field chemo-mechanical modelling of corrosion-induced cracking in reinforced concrete subjected to non-uniform chloride-induced corrosion. Theoret Appl Fract Mech 129:104233
59. Angst UM, Geiker MR, Michel A, Gehlen C, Wong H, Isgor OB, Elsener B, Hansson CM, François R, Hornbostel K, Polder R, Alonso MC, Sanchez M, Correia MJ, Criado M, Sagüés A, Buenfeld N (2017) The steel-concrete interface. Mater Struct 50:1–24
60. Wong HS, Angst UM, Geiker MR, Isgor OB, Elsener B, Michel A, Alonso MC, Correia MJ, Pacheco J, Gulikers J, Zhao Y, Criado M, Raupach M, Sørensen H, François

R, Mundra S, Rasol M, Polder R (2022) Methods for characterising the steel-concrete interface to enhance understanding of reinforcement corrosion: a critical review by RILEM TC 262-SCI. Mater Struct 55:124
61. Arndt D, Bangerth W, Davydov D, Heister T, Heltai L, Kronbichler M, Maier M, Pelteret JP, Turcksin B, Wells D (2021) The DEAL.II finite element library: design, features, and insights. Comput Math Appl 81:407–422
62. Bangerth W, Hartmann R, Kanschat G (2007) Deal II–a general-purpose object-oriented finite element library. ACM Trans Math Softw 33(2007):1–27
63. Baroghel-Bouny V, Mainguy M, Lassabatere T, Coussy O (1999) Characterization and identification of equilibrium and transfer moisture properties for ordinary and high-performance cementitious materials. Cem Concr Res 29:1225–1238
64. Michel A, Pease BJ (2018) Moisture ingress in cracked cementitious materials. Cem Concr Res 113:154–168
65. Liu P, Yu Z, Chen Y (2020) Carbonation depth model and carbonated acceleration rate of concrete under different environment. Cement Concr Compos 114:103736
66. Zhang Z, Thiery M, Baroghel-Bouny V (2016) Investigation of moisture transport properties of cementitious materials. Cem Concr Res 89:257–268
67. Powers TC, Brownyard TL (1946) Studies of the physical properties of hardened Portland cement paste, American Concrete Institute. ACI Special Publication SP-249, pp 265–617
68. Andrade C, Sarría J, Alonso C (1999) Relative humidity in the interior of concrete exposed to natural and artificial weathering. Cem Concr Res 29:1249–1259
69. Angulo Ramirez DE, Meira GR, Quattrone M, John VM (2023) A review on reinforcement corrosion propagation in carbonated concrete–influence of material and environmental characteristics. Cement Concr Compos 140:105085
70. Andrade C (2023) Role of oxygen and humidity in the reinforcement corrosion. Springer International Publishing
71. Hageman T, Andrade C, Martínez-Pañeda E (2023) Corrosion rates under charge-conservation conditions. Electrochim Acta 461:142624